Accurate coupled vibration analysis of a piezoelectric ceramic cylinder by the superposition method

Wenxiang Ding, Maxime Bavencoffe, Marc Lethiecq

Version of Record: https://www.sciencedirect.com/science/article/pii/S0041624X21001086
Manuscript_bc85325bdb12de239f16f9928c0f1801

Accurate Coupled Vibration Analysis of a Piezoelectric Ceramic Cylinder by the Superposition Method

Wenxiang Ding[1*], Maxime Bavencoffe, Marc Lethiecq

GREMAN UMR 7347 CNRS, Université de Tours, INSA Centre Val de Loire, 3 Rue de la Chocolaterie, Blois, France

Abstract

The radial and thickness extensional vibration modes in piezoelectric cylinders are always inevitably coupled due to the finite dimension, Poisson's ratio, and piezoelectric effect. In this paper, an analytical model based on the superposition method is developed to obtain the coupled dynamic response of a piezoelectric cylinder under an applied voltage. The problem can be described mathematically by three partial differential equations with mixed boundary conditions in the cylindrical coordinates system. To solve this, the problem is decomposed first into two building block – vibrations in radial and thickness directions. In each building block, the expressions of displacements and electric potential are assumed and then the induced dynamic responses, such as in-plane stress and electric displacements, are calculated. Finally, the vibration responses of the two building blocks are superimposed to satisfy the mixed boundary conditions using Fourier and Fourier-Bessel series expansions. Electrical impedance of a typical piezoelectric disk and frequency spectrum of piezoelectric cylinders of different diameter-to-thickness ratios are calculated by the present analytical method as well as by finite element method. Comparison shows an excellent agreement. This analytical model can be applied to material characterization and the design and the optimization of the active elements of piezoelectric devices.

Keywords: coupled vibration, analytical model, superposition method, electrical impedance, piezoelectric cylinder, finite element method

1. Introduction

Piezoceramic cylinders of different diameter-to-thickness (D/T) ratio have been widely used as the active element of ultrasonic transducers in many applications such as medical diagnostics, therapy, non-destructive evaluation (NDE), cleaning, atomizing

* Corresponding author.
Email address: wenxiang.ding@insa-cvl.fr (Wenxiang Ding), maxime.bavencoffe@insa-cvl.fr (Maxime Bavencoffe), marc.lethiecq@insa-cvl.fr (Marc Lethiecq).

liquids, drilling or milling materials, welding plastics as well as for many other purposes [1–4]. Depending on the material properties, the dimensions, the electric field applied and the poling direction, two principal vibration modes can be excited: the thickness extensional and the radial modes. One dimensional (1D) analytical models such as Van Dyke [5], Mason [6], or KLM [7] models have been proposed to characterize the dynamic response of the resonator when the diameter is much larger (i.e. ceramic disks) or much smaller (i.e. ceramic rods) than the thickness. However, these 1D models are not applicable to describe the coupling between radial and thickness modes. To address this, a two-dimensional (2D) or three-dimensional (3D) model is needed.

Due to its axisymmetric structure, the 3D vibration analysis of a piezoceramic cylinder can be reduced to a 2D problem in the cylindrical coordinate and can be described mathematically by a system of three partial differential equations (PDEs). The biggest difficulty of solving this problem lies in finding the appropriate forms for the unknown variables, i.e. mechanical displacements and electric potential, to satisfy both the differential equations and boundary conditions. Different kinds of potential functions were proposed in literature by Saito [8], Rajapakse et al [9,10], Wei and Chau [11,12], and Wang et al [13]. In these works, one or two potential functions were introduced, then the mechanical displacements and electric potential could be represented by a differential form to satisfy the equations of equilibrium and boundary conditions. However, they are only suitable in static regimes, not in dynamics. Recently, Ding et al [14] obtained the general solutions for coupled dynamic equations for a transversely isotropic piezoelectric medium by introducing two potential functions. Although the method was later extended to calculate the fundamental frequencies of a circular plate under open and closed circuit conditions [15], it is limited to the two specific boundary conditions, named as elastic simple support and rigid slipping support.

Approximate methods by virtue of weakening the coupling effect were developed lately by Brissaud [16,17], Iula [18], and Zhang [19]. The displacement along each propagation direction was considered as independent, i.e. only related to the corresponding coordinate, and the electrical quantities in non-polarized directions were assumed to be zero. The shear deformation was always neglected. In some ways, these assumptions did not satisfy the constitutive equations. A set of 2D second order approximate equations were deduced by Lee [20–22]. The calculated dispersion curves and resonance frequencies of piezoelectric crystal plates gave a good prediction. Similar second order equations were also developed by Li [23–25] and were applied to the vibration analysis of thin-film bulk acoustic wave resonators.

The coupling between vibration modes has been widely studied. Satisfactory results have been obtained in static regime for rectangular or cylindrical geometries. To the best of the author’s knowledge, the dynamic coupled response of a piezoelectric

ceramic under external electric field has not been established. In the present work, a complete analytical solution for coupled vibration in piezoelectric ceramic cylinders in vacuum is proposed based on the superposition method, which was first proposed by Gorman [26–28]. In section 2, the mathematical formulation is presented. Section 3 shows the coupling effect between radial and thickness modes and compares the results with those calculated by finite element (FE) method. Conclusions are given in section 4.

2. Mathematical Formulation

Here, a piezoelectric cylinder of thickness $2H$ and diameter $2R$ in vacuum is considered. Fig. 1 shows the coordinate system and dimensions. The poling direction is parallel to z-axis. The cartesian coordinates are x, y, and z. They correspond to r, θ, and z coordinates in a cylindrical system. An AC-voltage is applied between the top and bottom surfaces covered by metallic electrodes. Due to the axisymmetric structure, the 3D vibration analysis can be reduced to a 2D axisymmetric one as shown in Fig. 1(b).

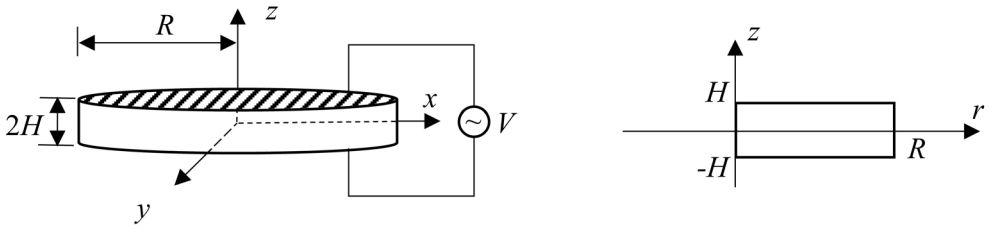

(a) (b)

Fig. 1. Schematic representation of the piezoelectric cylinder element. (a) three-dimensional (3D) model; (b) two-dimensional (2D) axisymmetric model.

The constitutive equations of a piezoelectric element can be expressed as [29]

$$\begin{aligned} T_\alpha &= c_{\alpha\beta}^E S_\beta - e_{i\alpha} E_i \\ D_i &= \varepsilon_{ij}^S E_j + e_{i\alpha} S_\alpha \end{aligned} \quad i, j = 1,2,3 \text{ and } \alpha, \beta = 1,...,6 \tag{1}$$

where $c_{\alpha\beta}^E$ are the elastic stiffness constants under constant electric field, $e_{i\alpha}$ are the piezoelectric constants, ε_{ij}^S are the dielectric constants under constant strain, T_α, S_β, E_i and D_i are the stress, strain, electric field and electric displacement, respectively.

For the 2D axisymmetric model, the interaction between θ and r/z-axis is omitted, thus $S_{r\theta} = S_{\theta z} = 0$ and $T_{r\theta} = T_{\theta z} = 0$. Based on this, the constitutive equations can be simplified and rewritten in the cylindrical coordinate system as follows

$$
\begin{aligned}
T_r &= c_{11}^E S_r + c_{12}^E S_\theta + c_{13}^E S_z - e_{31} E_z \\
T_\theta &= c_{12}^E S_r + c_{11}^E S_\theta + c_{13}^E S_z - e_{31} E_z \\
T_z &= c_{13}^E S_r + c_{13}^E S_\theta + c_{33}^E S_z - e_{33} E_z \\
T_{rz} &= c_{55}^E S_{rz} - e_{15} E_r \\
\mathrm{D}_r &= e_{15} S_{rz} + \varepsilon_{11}^S E_r \\
\mathrm{D}_z &= e_{31} S_r + e_{31} S_\theta + e_{33} S_z + \varepsilon_{33}^S E_z
\end{aligned} \tag{2}
$$

For axisymmetric structures, the strain and displacements are related by

$$
S_r = \frac{\partial u}{\partial r}, S_\theta = \frac{u}{r}, S_z = \frac{\partial w}{\partial z}, S_{rz} = \frac{\partial u}{\partial z} + \frac{\partial w}{\partial r} \tag{3}
$$

The electric fields are related to electric potential by

$$
E_r = -\frac{\partial \varphi}{\partial r}, E_z = -\frac{\partial \varphi}{\partial z} \tag{4}
$$

The coupled motion equations and Maxwell's equation for electrostatic field are

$$
\begin{aligned}
&\frac{\partial T_r}{\partial r} + \frac{\partial T_{rz}}{\partial z} + \frac{T_r - T_\theta}{r} = \rho \frac{\partial^2 u}{\partial t^2} \\
&\frac{\partial T_{rz}}{\partial r} + \frac{\partial T_z}{\partial z} + \frac{T_{rz}}{r} = \rho \frac{\partial^2 w}{\partial t^2} \\
&\frac{\partial D_r}{\partial r} + \frac{\partial D_z}{\partial z} + \frac{D_r}{r} = 0
\end{aligned} \tag{5}
$$

where ρ is the mass density of the material.

Substituting Eqs. (2)-(4) into Eq. (5) yields three coupled differential equations

$$
\begin{aligned}
&c_{11}^E \nabla^2 u - \rho \frac{\partial^2 u}{\partial t^2} + c_{55}^E \frac{\partial^2 u}{\partial z^2} + \left(c_{13}^E + c_{55}^E\right) \frac{\partial^2 w}{\partial r \partial z} + \left(e_{15} + e_{31}\right) \frac{\partial^2 \varphi}{\partial r \partial z} = 0 \\
&\left(c_{13}^E + c_{55}^E\right) \frac{\partial}{\partial z} \Delta u + c_{55}^E \Delta \frac{\partial w}{\partial r} - \rho \frac{\partial^2 w}{\partial t^2} + c_{33}^E \frac{\partial^2 w}{\partial z^2} + e_{15} \Delta \frac{\partial \varphi}{\partial r} + e_{33} \frac{\partial^2 \varphi}{\partial z^2} = 0 \\
&\left(e_{15} + e_{31}\right) \frac{\partial}{\partial z} \Delta u + e_{15} \Delta \frac{\partial w}{\partial r} + e_{33} \frac{\partial^2 w}{\partial z^2} - \varepsilon_{11}^S \Delta \frac{\partial \varphi}{\partial r} - \varepsilon_{33}^S \frac{\partial^2 \varphi}{\partial z^2} = 0
\end{aligned} \tag{6}
$$

where u, w are the displacements along r and z axes and φ is the electric potential. The operators Δ and ∇^2 are defined as

$$
\Delta = \frac{\partial}{\partial r} + \frac{1}{r}, \quad \nabla^2 = \frac{\partial}{\partial r} \Delta = \frac{\partial^2}{\partial r^2} + \frac{1}{r} \frac{\partial}{\partial r} - \frac{1}{r^2} \tag{7}
$$

Since there are no electrodes on the lateral surface, the electric displacement is equal to zero. In addition, the piezoelectric element is stress free and connected to an AC-voltage of angular frequency ω, therefore, the boundary conditions can be expressed as

$$
\begin{aligned}
&T_r = T_{rz} = D_r = 0 \qquad \text{at} \quad r = R \\
&T_z = T_{rz} = 0, \varphi = \pm \varphi_0 e^{j\omega t} \quad \text{at} \quad z = \pm H
\end{aligned} \tag{8}
$$

Owing to the piezoelectric effect, a symmetric constraint is imposed on the sample when an AC-voltage is applied. This leads to the displacement $u(r,z)$ being an even

function versus z coordinate while $w(r,z)$ and $\varphi(r,z)$ are odd functions of z. It can be summarized as follows

$$\begin{aligned} u(r,z) &= u(r,-z) \\ w(r,z) &= -w(r,-z) \\ \varphi(r,z) &= -\varphi(r,-z) \end{aligned} \tag{9}$$

2.1 General solution for the vibration responses

Since the piezoelectric element is axisymmetric with respect to z-axis and symmetric with respect to r-axis, a half part is chosen to be studied, as shown in Fig. 2(a). Two pairs of small circles indicate the symmetry condition along each side. As mentioned above, the major difficulty of solving the PDEs is to find an appropriate expression of the variables such that the PDEs and boundary conditions can be satisfied simultaneously. To address this, the model is divided into two building blocks as shown schematically in Fig. 2(b). In fact, the superposition method adopted here is a modified version of the method of separation of variables in mathematics. This separation process is tightly related to normal vibration modes in radial and thickness directions. The radial k_m and thickness k_n wavenumbers of vibration modes are induced in the first and second building blocks respectively (Fig 2.(b)). After that, their vibration responses are superimposed to satisfy the boundary conditions.

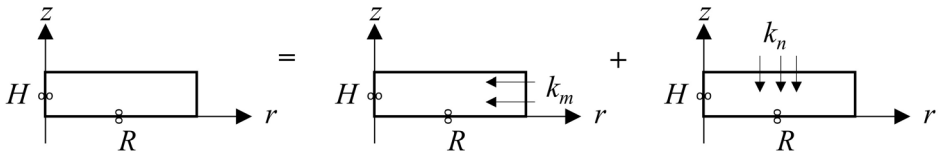

(a) (b)

Fig. 2. Schematic representation of a half of the 2D axisymmetric piezoelectric element (a) and two divided building blocks (b) for the general solution.

Let's now consider the first building block on the right of Fig. 2(b). Supposing that only the radial vibration modes are induced, the displacements and electric potential are expressed as follows [10,30]

$$\begin{aligned} u_m(r,z) &= U_m(z) J_1(k_m r) \\ w_m(r,z) &= W_m(z) J_0(k_m r) \quad (m = 1,2,...,+\infty) \\ \varphi_m(r,z) &= \psi_m(z) J_0(k_m r) \end{aligned} \tag{10}$$

where $J_0(k_m r)$ and $J_1(k_m r)$ are Bessel functions of the first kind of order zero and one, respectively. The wavenumber in the radial direction, k_m, is the m-th root of $J_0(k_m R) = 0$. For simplicity, the time component $e^{j\omega t}$ is omitted.

By substituting Eq. (10) into the coupled PDEs Eq. (6), we obtain

$$c_{55}^{E}U_m''(z)+\left(\rho\omega^2-c_{11}^{E}k_m^2\right)U_m(z)-\left(c_{55}^{E}+c_{13}^{E}\right)k_mW_m'(z)-k_m\left(e_{31}+e_{15}\right)\psi_m'(z)=0 \quad (11a)$$

$$\left(c_{13}^{E}+c_{55}^{E}\right)k_mU_m'(z)+c_{33}^{E}W_m''(z)+\left(\rho\omega^2-c_{55}^{E}k_m^2\right)W_m(z)+e_{33}\psi_m''(z)-e_{15}k_m^2\psi_m(z)=0 \quad (11b)$$

$$\left(e_{31}+e_{15}\right)k_mU_m'(z)+e_{33}W_m''(z)-e_{15}k_m^2W_m(z)-\varepsilon_{33}^{S}\psi_m''(z)+\varepsilon_{11}^{S}k_m^2\psi_m(z)=0 \quad (11c)$$

where the single apostrophe implies differentiation with respect to variable z once, double apostrophe implies twice, and so on. We can see that the variable r is separated from the PDEs in Eq. (6).

Solving Eqs. (11b) and (11c), the quantities $\psi_m(z)$ and $\psi_m''(z)$ can be expressed in terms of $U_m'(z)$, $W_m''(z)$, and $W_m(z)$. Combining this with Eq. (11a), we have

$$a_{m1}U_m''(z)+a_{m2}U_m(z)+a_{m3}W_m'''(z)+a_{m4}W_m'(z)=0 \quad (12a)$$

$$b_{m1}U_m'''(z)+b_{m2}U_m'(z)+b_{m3}W_m''(z)+b_{m4}W_m(z)=0 \quad (12b)$$

where the coefficients a_{mi} and b_{mi} (i = 1,2,3,4) are constants related to material properties, ω, and k_m. They are listed in Appendix (Eq. (A. 1)).

Differentiating Eq. (12b) once with respect to z and combining with Eq. (12a), the quantities $W_m'''(z)$ and $W_m'(z)$ can be expressed in terms of $U_m^{iv}(z)$, $U_m''(z)$, and $U_m(z)$. Let $W_m'''(z)$ be equal to $W_m'(z)$ differentiating twice with respect to z, a sixth order homogeneous differential equation involving only $U_m(z)$ and its derivatives is obtained

$$U_m^{vi}(z)+b_1U_m^{iv}(z)+c_1U_m''(z)+d_1U_m(z)=0 \quad (13)$$

where

$$b_1=\left(a_{m3}b_{m2}+a_{m4}b_{m1}-a_{m1}b_{m3}\right)/a_{m3}b_{m1},\ c_1=\left(a_{m4}b_{m2}-a_{m1}b_{m4}-a_{m2}b_{m3}\right)/a_{m3}b_{m1}$$
$$d_1=-a_{m2}b_{m4}/a_{m3}b_{m1}$$

Substituting the exponential function $e^{\lambda z}$ into Eq. (13), the characteristic equation related to the quantity $U_m(z)$ is obtained

$$\lambda^6+b_1\lambda^4+c_1\lambda^2+d_1=0 \quad (14)$$

For given ω and k_m, three roots with respect to λ^2 are given by the roots of a general cubic equation [31,32]. The roots of the characteristic equation are represented by three sets of square roots, denoted as

$$\lambda_i=\pm k_{mi}\left(i=1,2,3\right) \quad (15)$$

The frequency ω and wavenumber k_m are real, but λ_i^2 may be either real-positive, real-negative, or complex, which leads to several cases for the roots k_{mi}. In the present work, roots are considered as complex for the sake of generalization. Although we may

have + k_{mi} and - k_{mi} results, only the + k_{mi} need to be considered since they give the same solution after the conversion from exponential functions to hyperbolic ones [33].

The general solution $U_m(z)$, being an even function of z, can be expressed as

$$U_m(z) = \sum_{i=1}^{3} U_{mi} \cosh(k_{mi} z) \tag{16}$$

where U_{mi} are arbitrary constants.

Turning back to Eqs. (11) and (12), the quantities $W_m(z)$ and $\psi_m(z)$ can be expressed by $U_m(z)$

$$W_m(z) = b_2 U_m^v(z) + c_2 U_m'''(z) + d_2 U_m'(z) = \sum_{i=1}^{3} B_{mi} U_{mi} \sinh(k_{mi} z) \tag{17}$$

$$\psi_m(z) = b_3 U_m^v(z) + c_3 U_m'''(z) + d_3 U_m'(z) = \sum_{i=1}^{3} C_{mi} U_{mi} \sinh(k_{mi} z) \tag{18}$$

where

$$\begin{aligned}
&B_{mi} = b_2 k_{mi}^5 + c_2 k_{mi}^3 + d_2 k_{mi} \\
&b_2 = -b_{m1} a_{m3} b_{m3} / (-a_{m3} b_{m4} + a_{m4} b_{m3}) b_{m4}, \\
&c_2 = -b_{m1} / b_{m4} + (a_{m3} b_{m2} - a_{m1} b_{m3}) b_{m3} / (a_{m3} b_{m4} - a_{m4} b_{m3}) b_{m4} \\
&d_2 = -b_{m2} / b_{m4} - a_{m2} b_{m3}^2 / (a_{m3} b_{m4} - a_{m4} b_{m3}) b_{m4} \\
&C_{mi} = b_3 k_{mi}^5 + c_3 k_{mi}^3 + d_3 k_{mi} \\
&b_3 = a_{m3} b_{m1} (b_{m3} c_{m3} - b_{m4} c_{m2}) / (a_{m3} b_{m4} - a_{m4} b_{m3}) b_{m4} \\
&c_3 = -c_{m3} b_{m1} / b_{m4} + (c_{m3} b_{m3} - b_{m4} c_{m2})(a_{m3} b_{m2} - b_{m3} a_{m1}) / (a_{m3} b_{m4} - a_{m4} b_{m3}) b_{m4} \\
&d_3 = c_{m1} - c_{m3} b_{m2} / b_{m4} + a_{m2} b_{m3} (c_{m2} b_{m4} - b_{m3} c_{m3}) / (a_{m3} b_{m4} - a_{m4} b_{m3}) b_{m4}
\end{aligned}$$

and the coefficients c_{mi} (i = 1,2,3) are given in Appendix (Eq. (A. 2)).

Now let's turn to the second building block on the right of Fig. 2(b). The derivation is similar to the one of the first building block but slightly more complicated because of the cylindrical coordinate system. Therefore, for completeness sake, the derivation process is briefly presented here. In the second building block, the thickness vibrations are induced. To avoid confusion, a n-index is used for the notations of the displacements and electric potential [27,34]

$$\begin{aligned}
&u_n(r,z) = U_n(r)\cos(k_n z) \\
&w_n(r,z) = W_n(r)\sin(k_n z) \quad k_n = (2n-1)\frac{\pi}{2H} \text{ and } (n = 1,2,...,+\infty) \\
&\varphi_n(r,z) = \psi_n(r)\sin(k_n z)
\end{aligned} \tag{19}$$

Inserting this into Eq. (6), we have

$$c_{11}^E \nabla^2 U_n(r) + (\rho\omega^2 - c_{55}^E k_n^2) U_n(r) + (c_{13}^E + c_{55}^E) k_n W_n'(r) + (e_{31} + e_{15}) k_n \psi_n'(r) = 0 \tag{20a}$$

$$-\left(c_{13}^{E}+c_{55}^{E}\right)k_n\Delta U_n\left(r\right)+c_{55}^{E}\Delta W_n'\left(r\right)+\left(\rho\omega^2-c_{33}^{E}k_n^2\right)W_n\left(r\right)+e_{15}\Delta\psi_n'\left(r\right)-e_{33}k_n^2\psi_n\left(r\right)=0 \tag{20b}$$

$$-\left(e_{31}+e_{15}\right)k_n\Delta U_n\left(r\right)+e_{15}\Delta W_n'\left(r\right)-e_{33}k_n^2W_n\left(r\right)-\varepsilon_{11}^{S}\Delta\psi_n'\left(r\right)+\varepsilon_{33}^{S}k_n^2\psi_n\left(r\right)=0 \tag{20c}$$

where the apostrophe implies differentiation with respect to variable *r*. By combining the equations following a procedure similar to the previous case, we can eliminate the quantity $\psi_n\left(r\right)$. Then we have

$$\begin{aligned}&a_{n1}\nabla^2U_n\left(r\right)+a_{n2}U_n\left(r\right)+a_{n3}\nabla^2W_n'\left(r\right)+a_{n4}W_n'\left(r\right)=0\\&b_{n1}\Delta\nabla^2U_n\left(r\right)+b_{n2}\Delta U_n\left(r\right)+b_{n3}\Delta W_n'\left(r\right)+b_{n4}W_n\left(r\right)=0\end{aligned} \tag{21}$$

After combining these equations, we can eliminate the quantity $W_n\left(r\right)$ and obtain a differential equation involving only $U_n\left(r\right)$ and its derivatives

$$\nabla^6U_n\left(r\right)+b_1\nabla^4U_n\left(r\right)+c_1\nabla^2U_n\left(r\right)+d_1U_n\left(r\right)=0 \tag{22}$$

where the definition of the operator ∇^2 is given in Eq. (7).

For given ω and k_n, the three roots for $\nabla^2U_n\left(r\right)$ are denoted as k_{ni}^2, then, the solution of Eq. (22) is given by

$$U_n\left(r\right)=\sum_{i=1}^{3}U_{ni}I_1\left(k_{ni}r\right) \tag{23}$$

where U_{ni} are arbitrary constants and $I_1\left(k_{ni}r\right)$ is the modified Bessel function of the first kind of order one. The solutions for $W_n\left(r\right)$ and $\psi_n\left(r\right)$ can be expressed as

$$W_n\left(r\right)=b_2\Delta\nabla^4U_n\left(r\right)+c_2\Delta\nabla^2U_n\left(r\right)+d_2\Delta U_n\left(r\right)=\sum_{i=1}^{3}B_{ni}U_{ni}I_0\left(k_{ni}r\right) \tag{24}$$

$$\psi_n\left(r\right)=b_3\Delta\nabla^4U_n\left(r\right)+c_3\Delta\nabla^2U_n\left(r\right)+d_3\Delta U_n\left(r\right)=\sum_{i=1}^{3}C_{ni}U_{ni}I_0\left(k_{ni}r\right) \tag{25}$$

where $I_0\left(k_{ni}r\right)$ is the modified Bessel function of the first kind of order zero.

The coefficients a_{ni}, b_{ni} and c_{ni} (i = 1,2,3,4) for the second building block are detailed in the Appendix (Eq. (A. 3)). The other coefficients, such as b_i, c_i and d_i (i = 1,2,3), are exactly the same as those that appeared in the first building block. To obtain these coefficients, we need only to replace symbol *m* by *n*. For clarity, they are also given in the Appendix (Eq. (A. 4)).

With the solutions of the two building blocks above, the general solution for mechanical displacements and electric potential can be expressed as

$$
\begin{aligned}
u(r,z) &= \sum_{m=1}^{\infty} U_m(z) J_1(k_m r) + \sum_{n=1}^{\infty} U_n(r) \cos(k_n z) \\
&= \sum_{i=1}^{3} \left\{ \sum_{m=1}^{\infty} U_{mi} \cosh(k_{mi} z) J_1(k_m r) + \sum_{n=1}^{\infty} U_{ni} I_1(k_{ni} r) \cos(k_n z) \right\} \\
w(r,z) &= \sum_{m=1}^{\infty} W_m(z) J_0(k_m r) + \sum_{n=1}^{\infty} W_n(r) \sin(k_n z) \\
&= \sum_{i=1}^{3} \left\{ \sum_{m=1}^{\infty} B_{mi} U_{mi} \sinh(k_{mi} z) J_0(k_m r) + \sum_{n=1}^{\infty} B_{ni} U_{ni} I_0(k_{ni} r) \sin(k_n z) \right\} \\
\varphi(r,z) &= \sum_{m=1}^{\infty} \psi_m(z) J_0(k_m r) + \sum_{n=1}^{\infty} \psi_n(r) \sin(k_n z) \\
&= \sum_{i=1}^{3} \left\{ \sum_{m=1}^{\infty} C_{mi} U_{mi} \sinh(k_{mi} z) J_0(k_m r) + \sum_{n=1}^{\infty} C_{ni} U_{ni} I_0(k_{ni} r) \sin(k_n z) \right\}
\end{aligned}
\tag{26}
$$

The unknown coefficients U_{mi} and U_{ni} can be obtained after substituting the solution Eq. (26) into the boundary conditions Eq. (8). Once these coefficients are determined, the following expressions can be used to evaluate the dynamic vibration responses of stress, electric field, and electric displacements inside the element:

$$
\begin{aligned}
T_r(r,z) &= \sum_{i=1}^{3} \sum_{m=1}^{\infty} \left\{ \left[\left(c_{13}^E B_{mi} + e_{31} C_{mi} \right) k_{mi} + c_{11}^E k_m \right] J_0(k_m r) + \left(c_{12}^E - c_{11}^E \right) \frac{J_1(k_m r)}{r} \right\} \cosh(k_{mi} z) U_{mi} \\
&+ \sum_{i=1}^{3} \sum_{n=1}^{\infty} \left\{ \left[\left(c_{13}^E B_{ni} + e_{31} C_{ni} \right) k_n + c_{11}^E k_{ni} \right] I_0(k_{ni} r) + \left(c_{12}^E - c_{11}^E \right) \frac{I_1(k_{ni} r)}{r} \right\} \cos(k_n z) U_{ni} \\
T_\theta(r,z) &= \sum_{i=1}^{3} \sum_{m=1}^{\infty} \left\{ \left[\left(c_{13}^E B_{mi} + e_{31} C_{mi} \right) k_{mi} + c_{12}^E k_m \right] J_0(k_m r) + \left(c_{11}^E - c_{12}^E \right) \frac{J_1(k_m r)}{r} \right\} \cosh(k_{mi} z) U_{mi} \\
&+ \sum_{i=1}^{3} \sum_{n=1}^{\infty} \left\{ \left[\left(c_{13}^E B_{ni} + e_{31} C_{ni} \right) k_n + c_{12}^E k_{ni} \right] I_0(k_{ni} r) + \left(c_{11}^E - c_{12}^E \right) \frac{I_1(k_{ni} r)}{r} \right\} \cos(k_n z) U_{ni} \\
T_z(r,z) &= \sum_{i=1}^{3} \sum_{m=1}^{\infty} \left[\left(c_{33}^E B_{mi} + e_{33} C_{mi} \right) k_{mi} + c_{13}^E k_m \right] J_0(k_m r) \cosh(k_{mi} z) U_{mi} \\
&+ \sum_{i=1}^{3} \sum_{n=1}^{\infty} \left[\left(c_{33}^E B_{ni} + e_{33} C_{ni} \right) k_n + c_{13}^E k_{ni} \right] I_0(k_{ni} r) \cos(k_n z) U_{ni} \\
T_{rz}(r,z) &= \sum_{i=1}^{3} \sum_{m=1}^{\infty} \left[\left(-c_{55}^E B_{mi} - e_{15} C_{mi} \right) k_m + c_{55}^E k_{mi} \right] J_1(k_m r) \sinh(k_{mi} z) U_{mi} \\
&+ \sum_{i=1}^{3} \sum_{n=1}^{\infty} \left[\left(c_{55}^E B_{ni} + e_{15} C_{ni} \right) k_{ni} - c_{55}^E k_n \right] I_1(k_{ni} r) \sin(k_n z) U_{ni}
\end{aligned}
\tag{27}
$$

$$E_r(r,z)=\sum_{i=1}^{3}\sum_{m=1}^{\infty}C_{mi}k_m\sinh(k_{mi}z)J_1(k_mr)U_{mi}-\sum_{i=1}^{3}\sum_{n=1}^{\infty}C_{ni}k_{ni}I_1(k_{ni}r)\sin(k_nz)U_{ni}$$

$$E_z(r,z)=-\sum_{i=1}^{3}\sum_{m=1}^{\infty}C_{mi}k_{mi}\cosh(k_{mi}z)J_0(k_mr)U_{mi}-\sum_{i=1}^{3}\sum_{n=1}^{\infty}C_{ni}k_nI_0(k_{ni}r)\cos(k_nz)U_{ni}$$

$$\mathrm{D}_r(r,z)=\sum_{i=1}^{3}\sum_{m=1}^{\infty}\left[\left(-e_{15}B_{mi}+\varepsilon_{11}^{S}C_{mi}\right)k_m+e_{15}k_{mi}\right]\sinh(k_{mi}z)J_1(k_mr)U_{mi}$$
$$+\sum_{i=1}^{3}\sum_{n=1}^{\infty}\left[\left(e_{15}B_{ni}-\varepsilon_{11}^{S}C_{ni}\right)k_{ni}-e_{15}k_n\right]\sin(k_nz)I_1(k_{ni}r)U_{ni}$$

$$\mathrm{D}_z(r,z)=\sum_{i=1}^{3}\sum_{m=1}^{\infty}\left[\left(e_{33}B_{mi}-\varepsilon_{33}^{S}C_{mi}\right)k_{mi}+e_{31}k_m\right]\cosh(k_{mi}z)J_0(k_mr)U_{mi}$$
$$+\sum_{i=1}^{3}\sum_{n=1}^{\infty}\left[\left(e_{33}B_{ni}-\varepsilon_{33}^{S}C_{ni}\right)k_n+e_{31}k_{ni}\right]\cos(k_nz)I_0(k_{ni}r)U_{ni}$$

Contrary to the common assumption [16,18,19], the electric filed in radial direction E_r is not equal to zero. In addition, the symmetry property versus z-axis, shown in Eq. (9), can be verified here.

2.2 Determination of unknown coefficients

Assuming the number of vibration modes induced in the radial and thickness directions are K_1 (m = 1, 2,…,K_1) and K_2 (n = 1,2,…,K_2), there will be $3(K_1+K_2)$ linear equations for the $3(K_1+K_2)$ unknown coefficients of U_{mi} and U_{ni} by substituting the solutions into the boundary conditions of Eq. (8). The $3(K_1+K_2)$ linear equations can be presented in a concise way as

$$\begin{aligned}
&\sum_{m=1}^{K_1}\sum_{i=1}^{3}F_1^{mi}U_{mi}J_0(k_mr)=0 && \text{as}\quad T_z(z=\pm H)=0\\
&\sum_{n=1}^{K_2}\sum_{i=1}^{3}\left\{F_1^{ni}U_{ni}+\sum_{m=1}^{K_1}G_1^{mi}U_{mi}\right\}\cos(k_nz)=0 && \text{as}\quad T_r(r=R)=0\\
&\sum_{m=1}^{K_1}\sum_{i=1}^{3}\left\{F_2^{mi}U_{mi}+\sum_{n=1}^{K_2}G_2^{ni}U_{ni}\right\}J_1(k_mr)=0 && \text{as}\quad T_{rz}(z=\pm H)=0\\
&\sum_{n=1}^{K_2}\sum_{i=1}^{3}\left\{F_2^{ni}U_{ni}+\sum_{m=1}^{K_1}G_2^{mi}U_{mi}\right\}\sin(k_nz)=0 && \text{as}\quad T_{rz}(r=R)=0\\
&\sum_{m=1}^{K_1}\sum_{i=1}^{3}\left\{F_3^{mi}U_{mi}+\sum_{n=1}^{K_2}G_3^{ni}U_{ni}\right\}J_0(k_mr)=\varphi_0^{mi} && \text{as}\quad \varphi(z=\pm H)=\pm\varphi_0\\
&\sum_{n=1}^{K_2}\sum_{i=1}^{3}\left\{F_3^{ni}U_{ni}+\sum_{m=1}^{K_1}G_3^{mi}U_{mi}\right\}\sin(k_nz)=0 && \text{as}\quad D_r(r=R)=0
\end{aligned}\tag{28}$$

where F_j^{mi} and F_j^{ni} (j =1,2,3) can be easily obtained from Eq.(27); they are given by

$$
\begin{aligned}
F_1^{mi} &= \left[\left(c_{33}^E B_{mi} + C_{mi} e_{33}\right) k_{mi} + c_{13}^E k_m \right] \cosh\left(k_{mi} H\right) \\
F_1^{ni} &= \left[\left(c_{13}^E B_{ni} + C_{ni} e_{31}\right) k_n + c_{11}^E k_{ni} \right] I_0\left(k_{ni} R\right) + \left(c_{12}^E - c_{11}^E\right) I_1\left(k_{ni} R\right) / R \\
F_2^{mi} &= \left[\left(-c_{55}^E B_{mi} - e_{15} C_{mi}\right) k_m + c_{55}^E k_{mi} \right] \sinh\left(k_{mi} H\right) \\
F_2^{ni} &= \left[\left(c_{55}^E B_{ni} + e_{15} C_{ni}\right) k_{ni} - c_{55}^E k_n \right] I_1\left(k_{ni} R\right) \\
F_3^{mi} &= C_{mi} \sinh\left(k_{mi} H\right) \\
F_3^{ni} &= \left[\left(-\varepsilon_{11}^S C_{ni} + e_{15} B_{ni}\right) k_{ni} - e_{15} k_n \right] I_1\left(1, k_{ni} R\right)
\end{aligned}
\tag{29}
$$

and G_j^{mi}, G_j^{ni}, and φ_0^{mi} (j =1,2,3) are obtained using the Projection method [35]

$$
\begin{aligned}
G_1^{mi} &= \left(c_{12}^E - c_{11}^E\right) J_1\left(k_m R\right) 2 \int_0^H \cos(k_n z) \cosh\left(k_{mi} z\right) dz \Big/ RH \\
G_2^{ni} &= \left[\left(c_{55}^E B_{ni} + e_{15} C_{ni}\right) k_{ni} - c_{55}^E k_n \right] \sin\left(k_n H\right) \int_0^R r I_1\left(k_{ni} r\right) J_1\left(k_m r\right) dr \Big/ \left\| J_1\left(k_m r\right) \right\|^2 \\
G_2^{mi} &= \left[\left(-c_{55}^E B_{mi} - e_{15} C_{mi}\right) k_m + c_{55}^E k_{mi} \right] J_1\left(k_m R\right) 2 \int_0^H \sinh\left(k_{mi} z\right) \sin\left(k_n z\right) dz \Big/ H \\
G_3^{ni} &= C_{ni} \sin\left(k_n H\right) \int_0^R r I_0\left(k_{ni} r\right) J_0\left(k_m r\right) dr \Big/ \left\| J_0\left(k_m r\right) \right\|^2 \\
G_3^{mi} &= \left[\left(\varepsilon_{11}^S C_{mi} - e_{15} B_{mi}\right) k_m + e_{15} k_{mi} \right] J_1\left(k_m R\right) 2 \int_0^H \sinh\left(k_{mi} z\right) \sin\left(k_n z\right) dz \Big/ H
\end{aligned}
\tag{30}
$$

Eq. (28) shows that the stress T_z, T_{rz}, and electric potential φ at $z = \pm H$ can be expanded with the first kinds of Bessel functions of order 0, 1, and 0, respectively. The stress T_r, T_{rz}, and electric displacement D_r at $r = R$ can be expanded with cosine, sine, and sine functions, respectively. The boundary conditions are satisfied in the form of Fourier series and Fourier-Bessel series expansions. The summation of the expanded coefficients should be equal to zero except for the electric potential at $z = \pm H$.

The nonhomogeneous linear system in matrix notation can be described by

$$
\mathbf{A}\mathbf{x} = \mathbf{b} \tag{31}
$$

where $\mathbf{A}$ is a $3(K_1+K_2)\times 3(K_1+K_2)$ coefficient matrix, $\mathbf{x}$ is the unknown variable of U_{mi} and U_{ni}, and $\mathbf{b}$ is a $3(K_1+K_2)\times 1$ vector with K_1 non-zero elements related to φ_0.

For clarity, an example is shown here, where K_1 = 2 and K_2 = 3. The augmented matrix of the linear system is assembled and depicted schematically in Fig. 3. The elements denoted by an asterisk (*) are F_j^{mi} and F_j^{ni}, those denoted by a short solid bar (-) are G_j^{mi}, G_j^{ni} and φ_0^{mi}, and the rest are zeros. Once the constant φ_0 is known, all the coefficients can be determined.

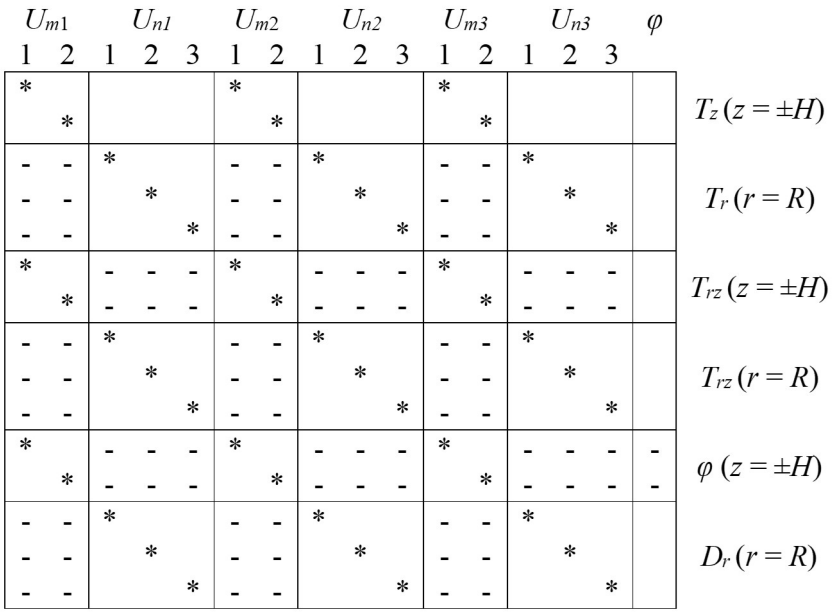

Fig. 3. Schematic representation of assembled augmented matrix of the system (* : F_j^{mi} and F_j^{ni}; -: G_j^{mi}, G_j^{ni}, and φ_0^{mi}).

2.3 Electrical impedance

The electrical impedance of piezoelectric material is defined as

$$Z=\frac{V}{I} \tag{32}$$

where V is the voltage applied between the electrodes and I is the electric current flowing through the sample.

Since the electric potential on the top and bottom electrodes are $\pm\varphi_0 e^{j\omega t}$, we have

$$V=\int_{-H}^{H} E_z dz=-\int_{-H}^{H}\frac{\partial\varphi}{\partial z}dz=-2\varphi_0 e^{j\omega t} \tag{33}$$

The electric current is defined by the differential of charge versus time. The charge on electrodes can be calculated by integrating the electric displacement density D_3 over the surface. Therefore,

$$I=\frac{\partial}{\partial t}\int_S D_3\left(r,H,t\right)dS=2\pi j\omega e^{j\omega t}\int_0^R D_z\left(r,H\right)rdr \tag{34}$$

Due to Eq. (19) and Eq. (27), $D_z\left(r,H\right)$ is given as

$$\mathrm{D}_z\left(r,H\right)=\sum_{i=1}^{3}\sum_{m=1}^{\infty}\left[\left(e_{33}B_{mi}-\varepsilon_{33}^{S}C_{mi}\right)k_{mi}+e_{31}k_m\right]\cosh\left(k_{mi}H\right)J_0\left(k_m r\right)U_{mi} \tag{35}$$

After obtaining all the unknown coefficients in Section 2.2, we can substitute them

into Eqs. (32)-(35), then the electrical impedance is determined. The time component $e^{j\omega t}$ and the constant φ_0 vanish in the results.

3. Results and Discussion

To verify the validity of the analytical model proposed here, the results are compared with those computed by a FE method. The FE analysis is carried out with COMSOL Multiphysics software in vacuum. Quadratic Lagrange rectangular elements with nine nodes are used and a frequency domain analysis is performed using 8 elements per shear wavelength for the highest frequency. The validation is performed in two parts: the electrical impedance and mode shape, represented by the spatial distribution of the mechanical displacements and electric potential, given in section 3.1. The predicted frequency spectrum comparison of different diameter-to-thickness ratios is shown in section 3.2.

Soft PZT materials provide high coupling factors and piezoelectric charge coefficients. They are widely used in applications such as medical diagnostic transducers, doppler flow meters, accelerometers and NDE. A soft PZ27 (Ferroperm Piezoceramics [36]) ceramic disk is used here, with diameter of 16 mm and thickness of 1.13 mm. An AC-voltage of ±1V is applied between the top and bottom electrodes. Material properties are listed in Table 1, where ρ is the density, $c_{\alpha\beta}^{E}$ are the elastic stiffness constants under constant electric field, $e_{i\alpha}$ are the piezoelectric constants, ε_{ij}^{S} are the dielectric constants under constant strain, δ_m and δ_e are respectively the mechanical loss factor and dielectric loss factor.

Table 1
Soft PZ27 piezoelectric material properties [36]

ρ(kg·m^{-3})	c_{11}^{E}(GPa)	c_{12}^{E}(GPa)	c_{13}^{E}(GPa)	c_{33}^{E}(GPa)	c_{44}^{E}(GPa)	c_{66}^{E}(GPa)
7800	147.4	104.9	93.7	112.6	23.0	21.25
e_{31}(C·m^{-2})	e_{33}(C·m^{-2})	e_{15}(C·m^{-2})	ε_{r11}^{S}	ε_{r33}^{S}	δ_m(%)	δ_e(%)
-3.1	16.0	11.6	913.7	1129.7	1.35	1.7

3.1 Electrical impedance and mode shape of a ceramic disk

Since the analytical model is based on Fourier and Fourier-Bessel series expansions, any desired degree of accuracy could be achieved by increasing the number of terms K_1 and K_2. To determine the values of K_1 and K_2, a convergence test for resonance frequency (f_r) is performed. Fig. 4 shows the variation of resonance frequency with

number of terms K_1, for all vibration modes in the frequency range between 0 and 2.4 MHz. The number of terms K_2 is set at 2 and the frequency resolution is set at 1kHz.

One can see that as the number of terms K_1 increases, more and more radial or coupling modes appear - in other words, to characterize high order radial harmonics and the coupling between thickness and radial modes in higher frequency ranges, K_1 needs to increase. One can also see that the calculated values of f_r converge vertically more or less to an asymptotic value as K_1 increases. The upper left area in Fig. 4, separated by a symbolic oblique solid line, can be considered as the area of convergence. It should be noted that in the case presented here (from 0 MHz to 2.4 MHz), 21 K_1 terms and 2 K_2 terms are sufficient to allow this asymptotic value to be obtained with good reproducibility.

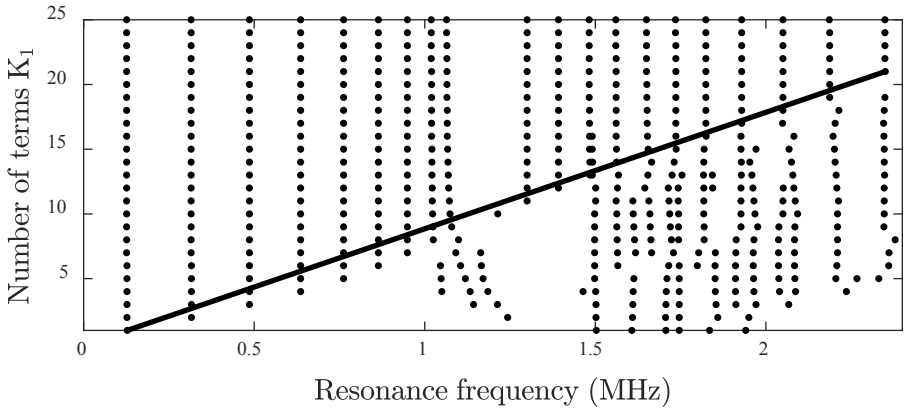

Fig. 4. The variation of resonance frequency with the number of terms K_1.

The electrical impedances for three different cases – $K_1 = K_2 = 1$ (Fig. 5(a)), $K_1 = 5$, $K_2 = 2$ (Fig. 5(b)), and $K_1 = 21$, $K_2 = 2$ (Fig. 5(c)) – are shown and compared with those of the FE method in Fig. 5. To measure the discrepancy, a mean absolute percentage deviation (MAPD) metric [37] is introduced and defined as

$$\text{MAPD}=\frac{1}{N}\sum_{i=1}^{N}\left|\frac{Z_{Analytical}(f_i)-Z_{FE}(f_i)}{Z_{FE}(f_i)}\right|\times 100 \tag{36}$$

where $Z(f_i)$ is the electrical impedance value at frequency f_i and N is the number of points evaluated.

The agreement between the analytical and the FE model improves and the MAPD decreases from Fig. 5(a) to Fig. 5(c). The MAPDs of the three sets of results are close to 55%, 15% and 2%, respectively. For a better illustration, the resonance and antiresonance frequencies in the third case are extracted and compared with those of the FE model. They are listed in Table 2, including the discrepancies in parentheses. The values are very close: the maximum discrepancy is inferior to 3 kHz for the frequency range calculated and the maximum deviation is under 2%, which occurs at the lower frequencies.

Table 2

Resonance and antiresonance frequencies of the piezoelectric disk from 0 to 2.4 MHz

Model	Resonance frequency (MHz)									
FE	0.124	0.315	0.485	0.636	0.762	0.864	0.949	1.018	1.062	1.300
Analytical	0.126	0.315	0.486	0.634	0.762	0.864	0.949	1.020	1.065	1.300
(deviation (%))	(1.61)	(0.00)	(0.21)	(0.00)	(0.00)	(0.00)	(0.00)	(0.20)	(0.28)	(0.00)
FE	1.392	1.481	1.560	1.649	1.736	1.825	1.930	2.051	2.187	/
Analytical	1.392	1.482	1.561	1.650	1.736	1.824	1.929	2.050	2.187	/
(deviation (%))	(0.00)	(0.07)	(0.06)	(0.06)	(0.00)	(0.05)	(0.05)	(0.05)	(0.00)	/
Model	Antiresonance frequency (MHz)									
FE	0.146	0.324	0.494	0.645	0.772	0.875	0.961	1.032	1.075	1.308
Analytical	0.147	0.325	0.494	0.645	0.772	0.875	0.961	1.033	1.078	1.308
(deviation (%))	(0.68)	(0.31)	(0.00)	(0.00)	(0.00)	(0.00)	(0.00)	(0.10)	(0.28)	(0.00)
FE	1.404	1.512	1.578	1.667	1.804	1.891	1.953	2.070	2.201	/
Analytical	1.404	1.512	1.578	1.668	1.804	1.891	1.953	2.068	2.199	/
(deviation (%))	(0.00)	(0.00)	(0.00)	(0.06)	(0.00)	(0.00)	(0.00)	(0.10)	(0.10)	/

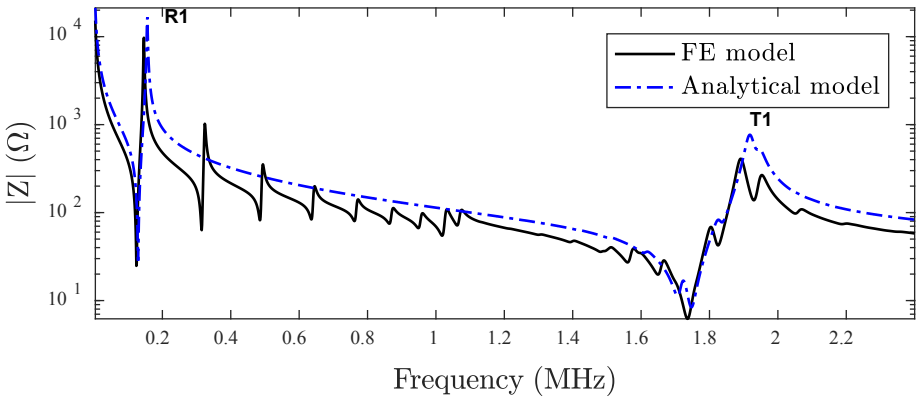

(a)

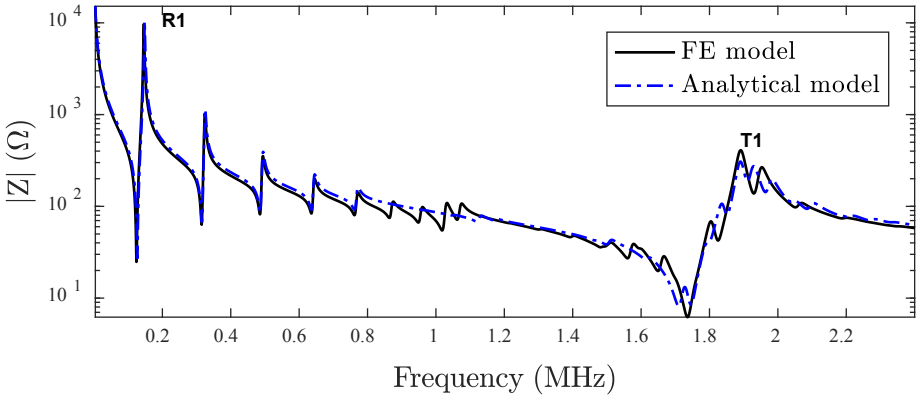

(b)

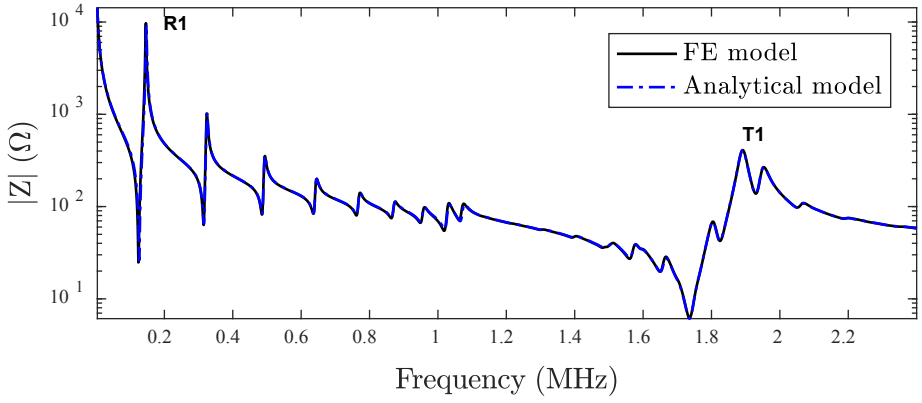

(c)

Fig. 5. The modulus of electrical impedance of the piezoelectric disk obtained by using different number of terms. (a) $K_1 = 1$, $K_2 = 1$; (b) $K_1 = 5$, $K_2 = 2$; (c) $K_1 = 21$, $K_2 = 2$. Solid lines refer to the results of the FE model and chain dotted lines refer to the results of the analytical model.

The mode shapes of total displacement U, defined as $\sqrt{u^2 + w^2}$, and electric potential φ are calculated by Eq. (26). Results at the antiresonance frequency of the fundamental radial (R1) and thickness (T1) modes, as labelled in Fig. 5, are shown in Fig. 6 and Fig. 7. Comparison shows an excellent agreement, in accordance with [38], including not only the spatial distribution but also the amplitudes (i.e. total displacement and electric potential respectively). The vibration pattern of R1 mode can be easily recognized from Fig. 6(a) & (c): the piezoceramic disk extends in the radial direction while keeping close to constant in the thickness direction. The electric potential distribution, as shown in Fig. 6(b) & (d), is uniform in the radial direction but linear in its poling direction, i.e. the thickness direction. From Fig. 7(a) & (c) we can see that the vibration of T1 mode is predominant in the thickness direction but is greatly influenced by the higher harmonics of radial modes. Additionally, the displacement is higher at the surface center than at the periphery. Owing to the piezoelectric effect, the distribution of electric potential of T1 mode (Fig. 7(b) & (d)) is similar to that of displacement. Besides, although an AC-voltage of ±1V is applied between the top and bottom electrodes in the poling direction, the electric potential inside some locations of the element exceeds this range and is more than ±2V.

In addition, compared to the FE method, the analytical method shows a great advantage in terms of computational efficiency: the calculation time is reduced from the FE method's 181.3s to only 2.8s for the third case. Thus, a comparable accuracy is attained 64 times faster.

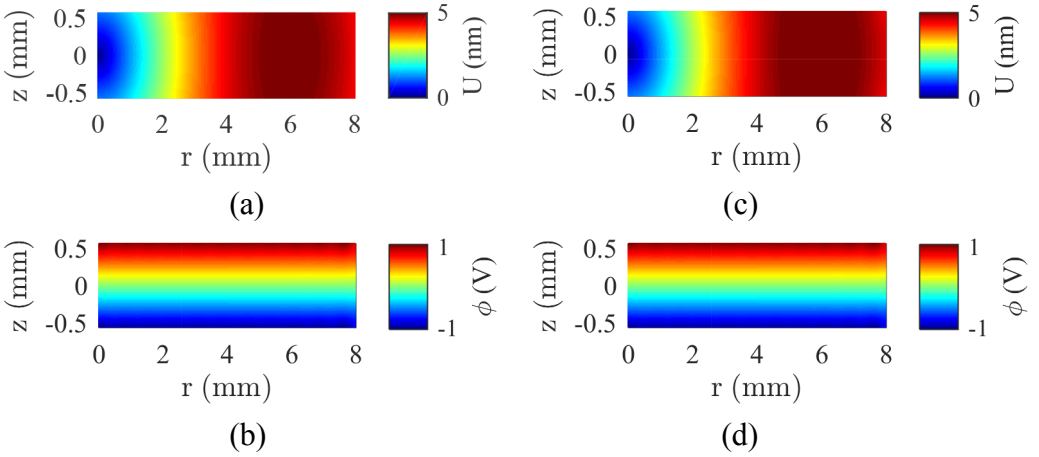

Fig. 6. The total displacement and electric potential of the piezoelectric ceramic disk at the antiresonance frequency of the first radial (R1) mode. (a)-(b) indicate results of the FE model; (c)-(d) indicate results of analytical model with $K_1 = 21$ and $K_2 = 2$.

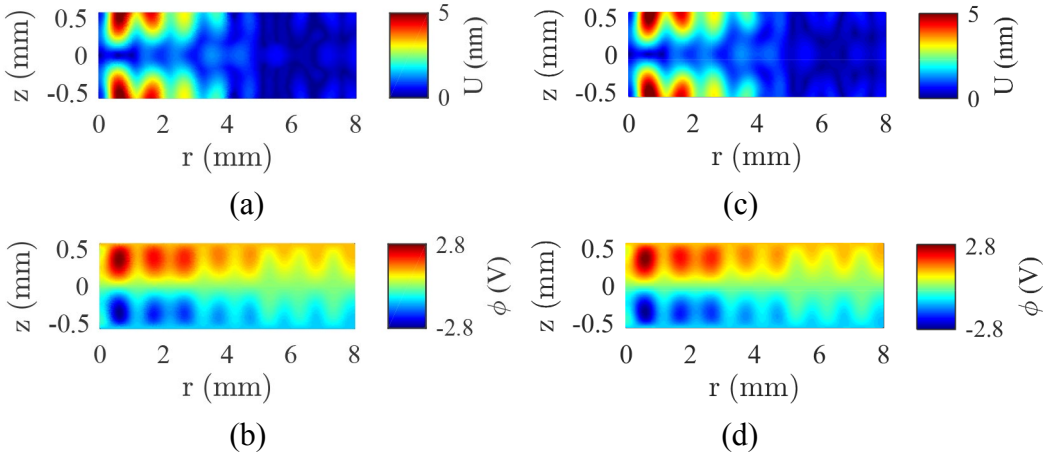

Fig. 7. The total displacement and electric potential of the piezoelectric ceramic disk at the antiresonance frequency of the first thickness (T1) mode. (a)-(b) indicate results of the FE model; (c)-(d) indicate results of analytical model with $K_1 = 21$ and $K_2 = 2$.

3.2 Frequency spectrum

The present analytical model has been extended to predict the frequency spectrum of PZ27 piezoelectric disks, that is, relations between resonance frequencies and diameter-to-thickness (D/T) ratios, as shown in Fig. 8. Here, the material is assumed to be lossless. The D/T ratio varies from 0.2 to 20 with a step of 0.05 while the thickness is kept constant as 1.13 mm. This range covers most of the piezoelectric element geometries used in ultrasonic transducers. Since the electrical impedance is inversely proportional to the electrode area, the amplitude is first normalized to a unit area and then normalized between 0 and 1. The resonance amplitude of the vibration modes is represented by the color scale in Fig. 8. Besides, to avoid a convergence analysis in each

case, K_1 and K_2 are set at 30 and 2 for D/T ratios larger than 5 and are both set at 10 for the other cases.

The overall vibration pattern shown in Fig. 8 is similar to the measured or calculated frequency spectrum by FE model [38–41]. Results from the FE model, marked by black circles, are superimposed over analytical ones in Fig. 8. An excellent agreement can be observed. Several features are also clearly shown in the frequency spectrum. The three "terraces", as mentioned in [40], are noted as edge modes (E), thickness shear modes (TS), and thickness extensional modes (TE). Their locations are also indicated by the arrows on the right of the plot area. The TS terrace is the most obvious in Fig. 8. It is close to flat and the number of TS modes increases as D/T ratio increases. The TE terrace is obviously characterized by its high resonance amplitude, i.e. the lighter color. The E terrace can be speculated because the rate of change of resonance frequency with D/T ratio is reduced in this region.

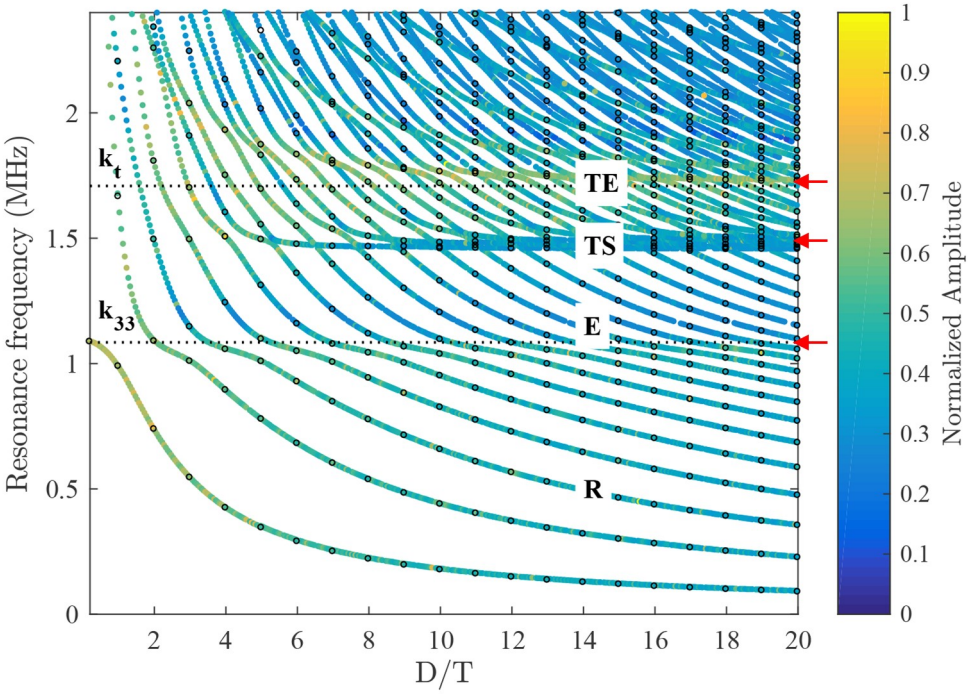

Fig. 8. Resonance frequencies vs diameter-to-thickness ratios D/T of PZ27 disks with constant thickness 1.13 mm. Gray points, scaled by normalized amplitude, are results of the analytical model and black circle are results of the FE model.

The two horizontal dotted lines, labeled as k_{33} and k_t in Fig. 8, are results from the one-dimensional (1D) KLM model [7]. As D/T ratio approaches 0, the piezoelectric cylinder turns into a long rod with small section poled along its largest dimension, which can be modelled by KLM model with electromechanical coupling coefficient equal to k_{33} (D/T $\rightarrow$ 0). As D/T ratio approaches 20 or even higher, the cylinder turns into a thin disk poled along its thickness. It can be modelled by KLM with coupling

coefficient k_t (D/T $\rightarrow$ $+\infty$). The electrical impedances of these two extreme cases calculated by two analytical models are shown in Fig. 9. In Fig. 9(a), only the length expander (LE) mode exists in the frequency range (0 to 2.4 MHz), and the resonance frequency is close to 1.1 MHz. In Fig. 9(b), the TE mode is highly perturbated by other modes, and the resonance frequency is around 1.7 MHz. These two resonance frequencies, calculated by KLM model, could be considered as two asymptotic bounds for real situation: an upper bound (D/T $\rightarrow$ 0) and a lower bound (D/T $\rightarrow$ $+\infty$). They are found by our analytical model with a discrepancy of less than 1%. This small discrepancy is linked to the D/T ratio: contrary to KLM model, the radial contribution is taken into account in our analytical model by means of a finite value of D/T. Plus, compared with KLM model, the analytical model proposed here can describe not only the two fundamental vibrations in radial and thickness directions but also the coupled modes such as E and TS modes.

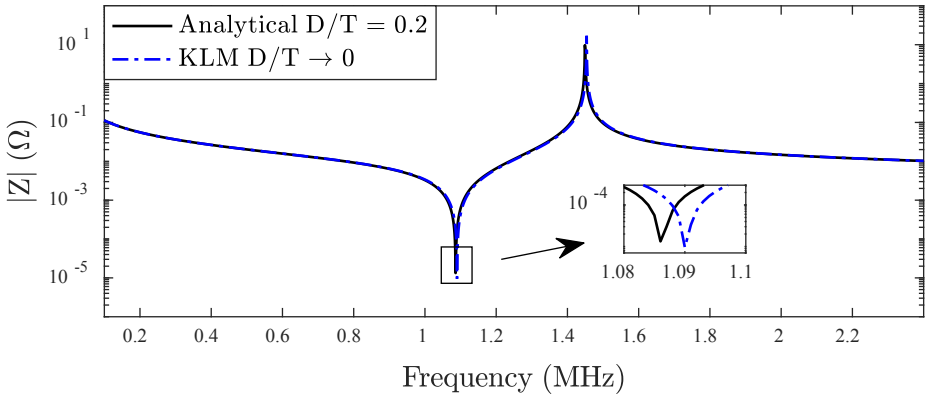

(a)

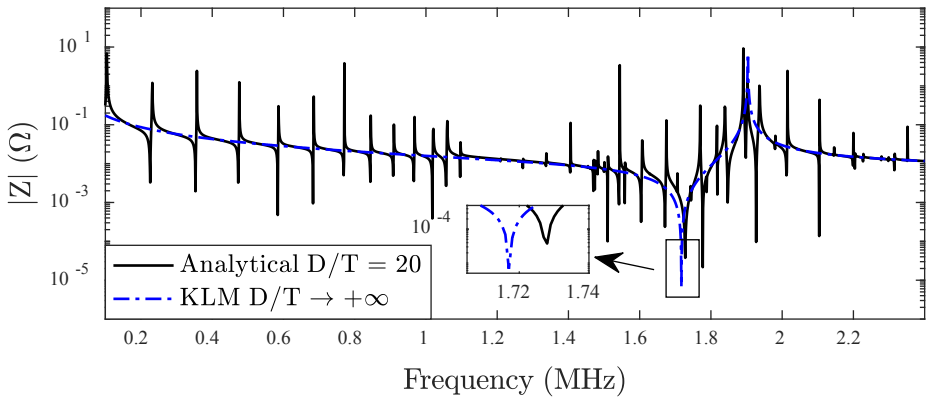

(b)

Fig. 9. The modulus of electrical impedance of a long piezoelectric rod (a) and a thin piezoelectric disk (b). Solid lines refer to the results of the present analytical model and chain dotted lines refer to the results of KLM model.

4. Conclusions

In this paper, accurate analytical solutions have been obtained for coupled vibrations in piezoceramic cylinders based on superposition method. The problem has been divided into two building blocks – vibrations in radial and thickness directions – and solution in each building block are superimposed to form the final solution. The mixed boundary conditions are satisfied using Fourier and Fourier-Bessel series expansions.

The solutions for the in-plane dynamic responses, such as stress, electric field, and electric displacements, are formulated. Electrical impedance and mode shape of a typical size PZ27 piezoelectric disk, as well as the frequency spectrum of the same material but with different diameter-to-thickness ratios are calculated and compared to those of the FE method. An excellent agreement is observed. The mean absolute percentage deviation (MAPD) of the electrical impedance curve is inferior to 2%. In addition, the analytical method shows a great advantage in terms of computational efficiency – it is over 64 times faster than FE one for the same level of precision. Furthermore, comparison shows that the present analytical method is more accurate than KLM model: not only the radial and thickness modes but also the other coupled modes can be characterized using the analytical model proposed here.

The present analytical model can be used to help with the characterization of some material parameters but also for the design and the optimization of the active elements of piezoelectric devices, such as ultrasonic transducers.

Acknowledgements

The work was financially supported by the China Scholarship Council (CSC) through the cooperation program UT-INSA (France).

The authors thank Meggitt A/S Denmark for providing the Ferroperm Piezoceramic samples.

Appendix

The constants a_{mi} and b_{mi} (i = 1,2,3,4) appearing in Eq. (12) are defined by

$$a_{m1} = \frac{\left(c_{13}^E + c_{55}^E\right)\varepsilon_{33}^S + \left(e_{31} + e_{15}\right)e_{33}}{\left(e_{15}\varepsilon_{33}^S - e_{33}\varepsilon_{11}^S\right)k_m} - \frac{c_{55}^E}{\left(e_{31} + e_{15}\right)k_m}$$

$$a_{m2} = \frac{c_{11}^E k_m}{e_{31} + e_{15}} - \frac{\omega^2 \rho}{\left(e_{31} + e_{15}\right)k_m}$$

$$a_{m3}=\frac{c_{33}^{E}\varepsilon_{33}^{S}+e_{33}^{2}}{k_m^{2}\left(e_{15}\varepsilon_{33}^{S}-e_{33}\varepsilon_{11}^{S}\right)}$$

$$a_{m4}=\frac{c_{55}^{E}+c_{13}^{E}}{e_{31}+e_{15}}-\frac{e_{15}e_{33}}{e_{15}\varepsilon_{33}^{S}-e_{33}\varepsilon_{11}^{S}}+\frac{\left(\rho\omega^{2}-c_{55}^{E}k_m^{2}\right)\varepsilon_{33}^{S}}{\left(e_{15}\varepsilon_{33}^{S}-e_{33}\varepsilon_{11}^{S}\right)k_m^{2}} \qquad \text{(A. 1)}$$

$$b_{m1}=\frac{e_{33}c_{55}^{E}}{\left(e_{31}+e_{15}\right)k_m}$$

$$b_{m2}=\left(-\frac{e_{33}c_{11}^{E}}{e_{31}+e_{15}}-\frac{\left(c_{55}^{E}+c_{13}^{E}\right)e_{33}\varepsilon_{11}^{S}+\left(e_{31}+e_{15}\right)e_{15}e_{33}}{e_{15}\varepsilon_{33}^{S}-e_{33}\varepsilon_{11}^{S}}\right)k_m+\frac{e_{33}\rho\omega^{2}}{\left(e_{31}+e_{15}\right)k_m}$$

$$b_{m3}=c_{33}^{E}-\frac{e_{33}\left(c_{55}^{E}+c_{13}^{E}\right)}{e_{31}+e_{15}}-\frac{e_{15}\left(c_{33}^{E}\varepsilon_{33}^{S}+e_{33}^{2}\right)}{e_{15}\varepsilon_{33}^{S}-e_{33}\varepsilon_{11}^{S}}$$

$$b_{m4}=\frac{\left(c_{55}^{E}\varepsilon_{11}^{S}+e_{15}^{2}\right)e_{33}}{e_{15}\varepsilon_{33}^{S}-e_{33}\varepsilon_{11}^{S}}k_m^{2}-\frac{e_{33}\varepsilon_{11}^{S}}{e_{15}\varepsilon_{33}^{S}-e_{33}\varepsilon_{11}^{S}}\omega^{2}\rho$$

The constants c_{mi} (i = 1,2,3) appearing in Eq. (18) are defined by

$$c_{m1}=\frac{\left(c_{13}^{E}+c_{55}^{E}\right)\varepsilon_{33}^{S}+\left(e_{31}+e_{15}\right)e_{33}}{\left(e_{15}\varepsilon_{33}^{S}-e_{33}\varepsilon_{11}^{S}\right)k_m}$$

$$c_{m2}=\frac{c_{33}^{E}\varepsilon_{33}^{S}+e_{33}^{2}}{k_m^{2}\left(e_{15}\varepsilon_{33}^{S}-e_{33}\varepsilon_{11}^{S}\right)} \qquad \text{(A. 2)}$$

$$c_{m3}=-\frac{c_{55}^{E}\varepsilon_{33}^{S}+e_{15}e_{33}}{e_{15}\varepsilon_{33}^{S}-e_{33}\varepsilon_{11}^{S}}+\frac{\omega^{2}\rho\varepsilon_{33}^{S}}{\left(e_{15}\varepsilon_{33}^{S}-e_{33}\varepsilon_{11}^{S}\right)k_m^{2}}$$

The coefficients a_{ni}, b_{ni} and c_{ni} (i = 1,2,3,4) for the second building block (on the right of Fig. 2(b))) are defined as

$$a_{n1}=\frac{\left(c_{13}^{E}+c_{55}^{E}\right)\varepsilon_{11}^{S}+\left(e_{31}+e_{15}\right)e_{15}}{\left(e_{15}\varepsilon_{33}^{S}-e_{33}\varepsilon_{11}^{S}\right)k_n}+\frac{c_{11}^{E}}{\left(e_{31}+e_{15}\right)k_n}$$

$$a_{n2}=-\frac{c_{55}^{E}k_n}{e_{31}+e_{15}}+\frac{\rho\omega^{2}}{\left(e_{31}+e_{15}\right)k_n}$$

$$a_{n3}=-\frac{c_{55}^{E}\varepsilon_{11}^{S}+e_{15}^{2}}{k_n^{2}\left(e_{15}\varepsilon_{33}^{S}-e_{33}\varepsilon_{11}^{S}\right)}$$

$$a_{n4}=\frac{c_{33}^{E}\varepsilon_{11}^{S}+e_{15}e_{33}}{e_{15}\varepsilon_{33}^{S}-e_{33}\varepsilon_{11}^{S}}+\frac{c_{13}^{E}+c_{55}^{E}}{e_{31}+e_{15}}-\frac{\omega^{2}\rho\varepsilon_{11}^{S}}{\left(e_{15}\varepsilon_{33}^{S}-e_{33}\varepsilon_{11}^{S}\right)k_n^{2}}$$

$$b_{n1}=-\frac{e_{15}c_{11}^{E}}{\left(e_{31}+e_{15}\right)k_n}$$

$$
\begin{aligned}
b_{n2} &= \left(\frac{e_{15}c_{55}^{E}}{e_{31}+e_{15}} - \frac{\left(c_{13}^{E}+c_{55}^{E}\right)e_{15}\varepsilon_{33}^{S}+\left(e_{31}+e_{15}\right)e_{15}e_{33}}{e_{15}\varepsilon_{33}^{S}-e_{33}\varepsilon_{11}^{S}} \right) k_n - \frac{e_{15}\omega^2\rho}{\left(e_{31}+e_{15}\right)k_n} \\
b_{n3} &= c_{55}^{E} + \frac{e_{33}\left(c_{55}^{E}\varepsilon_{11}^{S}+e_{15}^{2}\right)}{e_{15}\varepsilon_{33}^{S}-e_{33}\varepsilon_{11}^{S}} - \frac{e_{15}\left(c_{13}^{E}+c_{55}^{E}\right)}{e_{31}+e_{15}} \\
b_{n4} &= \frac{\left(c_{33}^{E}\varepsilon_{33}^{S}-e_{33}^{2}\right)e_{15}}{e_{15}\varepsilon_{33}^{S}-e_{33}\varepsilon_{11}^{S}}k_n^2 + \frac{e_{15}\varepsilon_{33}^{S}}{e_{15}\varepsilon_{33}^{S}-e_{33}\varepsilon_{11}^{S}}\omega^2\rho \\
c_{n1} &= \frac{\left(c_{13}^{E}+c_{55}^{E}\right)\varepsilon_{11}^{S}+e_{15}\left(e_{31}+e_{15}\right)}{\left(e_{15}\varepsilon_{33}^{S}-e_{33}\varepsilon_{11}^{S}\right)k_n} \\
c_{n2} &= -\frac{c_{55}^{E}\varepsilon_{11}^{S}+e_{15}^{2}}{k_n^2\left(e_{15}\varepsilon_{33}^{S}-e_{33}\varepsilon_{11}^{S}\right)} \\
c_{n3} &= \frac{c_{33}^{E}\varepsilon_{11}^{S}+e_{15}e_{33}}{e_{15}\varepsilon_{33}^{S}-e_{33}\varepsilon_{11}^{S}} - \frac{\omega^2\rho\varepsilon_{11}^{S}}{\left(e_{15}\varepsilon_{33}^{S}-e_{33}\varepsilon_{11}^{S}\right)k_n^2}
\end{aligned}
\tag{A. 3}
$$

and the other coefficients b_i, c_i and d_i (i = 1,2,3) are defined as

$$
\begin{aligned}
b_1 &= \left(-a_{n1}b_{n3}+a_{n3}b_{n2}+a_{n4}b_{n1}\right)/b_{n1}a_{n3} \\
c_1 &= \left(-a_{n1}b_{n4}-a_{n2}b_{n3}+a_{n4}b_{n2}\right)/b_{n1}a_{n3} \\
d_1 &= -a_{n2}b_{n4}/a_{n3}b_{n1} \\
B_{ni} &= b_2k_{ni}^5 + c_2k_{ni}^3 + d_2k_{ni} \\
b_2 &= b_{n1}a_{n3}b_{n3}/b_{n4}\left(a_{n3}b_{n4}-a_{n4}b_{n3}\right) \\
c_2 &= -b_{n1}/b_{n4} + \left(a_{n3}b_{n2}-a_{n1}b_{n3}\right)b_{n3}/\left(a_{n3}b_{n4}-a_{n4}b_{n3}\right)b_{n4} \\
d_2 &= -b_{n2}/b_{n4} - a_{n2}b_{n3}^2/\left(a_{n3}b_{n4}-a_{n4}b_{n3}\right)b_{n4} \\
C_{ni} &= b_3k_{ni}^5 + c_3k_{ni}^3 + d_3k_{ni} \\
b_3 &= a_{n3}b_{n1}\left(b_{n3}c_{n3}-b_{n4}c_{n2}\right)/\left(a_{n3}b_{n4}-a_{n4}b_{n3}\right)b_{n4} \\
c_3 &= -c_{n3}b_{n1}/b_{n4} + \left(c_{n3}b_{n3}-b_{n4}c_{n2}\right)\left(a_{n3}b_{n2}-b_{n3}a_{n1}\right)/\left(a_{n3}b_{n4}-a_{n4}b_{n3}\right)b_{n4} \\
d_3 &= c_{n1}-c_{n3}b_{n2}/b_{n4} + a_{n2}b_{n3}\left(c_{n2}b_{n4}-b_{n3}c_{n3}\right)/\left(a_{n3}b_{n4}-a_{n4}b_{n3}\right)b_{n4}
\end{aligned}
\tag{A. 4}
$$

References

[1] A.D. Farmer, A.F. Collings, G.J. Jameson, The application of power ultrasound to the surface cleaning of silica and heavy mineral sands, Ultrasonics Sonochemistry. 7 (2000) 243–247. https://doi.org/10.1016/S1350-4177(00)00057-2.

[2] P. Marechal, F. Levassort, J. Holc, L.-P. Tran-Huu-Hue, M. Kosec, M. Lethiecq, High-frequency transducers based on integrated piezoelectric thick films for medical imaging, IEEE Transactions on Ultrasonics, Ferroelectrics, and Frequency

Control. 53 (2006) 1524–1533. https://doi.org/10.1109/TUFFC.2006.1665110.

[3] M. Lethiecq, F. Levassort, D. Certon, L.P. Tran-Huu-Hue, Piezoelectric transducer design for medical diagnosis and NDE, in: Piezoelectric and Acoustic Materials for Transducer Applications, Springer, 2008: pp. 191–215.

[4] M. Bavencoffe, N. Tembhurnikar, B. Negulescu, J. Wolfman, G. Feuillard, Modelling and experimental measurements of the mechanical response of piezoelectric structures from millimetre to micrometre, Advances in Applied Ceramics. 117 (2018) 285–290. https://doi.org/10.1080/17436753.2018.1458475.

[5] K.S.V. Dyke, The Piezo-Electric Resonator and Its Equivalent Network, Proceedings of the IRE. 16 (1928) 742–764. https://doi.org/10.1109/jrproc.1928.221466.

[6] W.P. Mason, Electromechanical transducers and wave filters, 2nd ed., D. Van Nostrand Company, 1948.

[7] R. Krimholtz, D.A. Leedom, G.L. Matthaei, New equivalent circuits for elementary piezoelectric transducers, Electronics Letters. 6 (1970) 398–399. https://doi.org/10.1049/el:19700280.

[8] H. SAITO, The Axially Symmetrical Deformation of a Short Circular Cylinder, Transactions of the Japan Society of Mechanical Engineers. 18 (1952) 21–28. https://doi.org/10.1299/kikai1938.18.68_21.

[9] R.K.N.D. Rajapakse, Y. Chen, T. Senjuntichai, Electroelastic field of a piezoelectric annular finite cylinder, International Journal of Solids and Structures. 42 (2005) 3487–3508. https://doi.org/10.1016/j.ijsolstr.2004.10.019.

[10] Y. Chen, R.K.N.D. Rajapakse, Electric Charge Loading of a Piezoelectric Solid Cylinder, in: IUTAM Symposium on Mechanics and Reliability of Actuating Materials, Springer Netherlands, Dordrecht, 2006: pp. 164–174.

[11] X.X. Wei, K.T. Chau, R.H.C. Wong, Analytic Solution for Axial Point Load Strength Test on Solid Circular Cylinders, Journal of Engineering Mechanics. 125 (1999) 1349–1357. https://doi.org/10.1061/(asce)0733-9399(1999)125:12(1349).

[12] X.X. Wei, K.T. Chau, Analytic Solution for Finite Transversely Isotropic Circular Cylinders under the Axial Point Load Test, Journal of Engineering Mechanics. 128 (2002) 209–219. https://doi.org/10.1061/(asce)0733-9399(2002)128:2(209).

[13] Z. Wang, G. Chen, A general solution and the application of space axisymmetric problem in piezoelectric material, Applied Mathematics and Mechanics. 15 (1994) 615–626. https://doi.org/10.1007/bf02451611.

[14] H. Ding, B. Chen, J. Liang, General solutions for coupled equations for piezoelectric media, International Journal of Solids and Structures. 33 (1996) 2283–2298. https://doi.org/10.1016/0020-7683(95)00152-2.

[15] H. Ding, R. Xu, W. Chen, Exact solutions for free vibration of transversely isotropic piezoelectric circular plates, Acta Mechanica Sinica. 16 (2000) 141–147. https://doi.org/10.1007/bf02486706.

[16] M. Brissaud, Characterization of piezoceramics, IEEE Transactions on Ultrasonics, Ferroelectrics, and Frequency Control. 38 (1991) 603–617. https://doi.org/10.1109/58.108859.

[17] M. Brissaud, Three-dimensional modeling of piezoelectric materials, IEEE Transactions on Ultrasonics, Ferroelectrics, and Frequency Control. 57 (2010) 2051–2065. https://doi.org/10.1109/TUFFC.2010.1653.

[18] A. Iula, N. Lamberti, M. Pappalardo, An approximated 3-D model of cylinder-shaped piezoceramic elements for transducer design, IEEE Transactions on Ultrasonics, Ferroelectrics and Frequency Control. 45 (1998) 1056–1064. https://doi.org/10.1109/58.710588.

[19] X. Zhang, S. Lin, Y. Wang, Three-dimensional coupled vibration theory for the longitudinally polarized piezoelectric ceramic tube, Applied Acoustics. 91 (2015) 59–63. https://doi.org/10.1016/j.apacoust.2014.12.005.

[20] P.C.Y. Lee, J.D. Yu, W.S. Lin, A new two-dimensional theory for vibrations of piezoelectric crystal plates with electroded faces, Journal of Applied Physics. 83 (1998) 1213–1223. https://doi.org/10.1063/1.366818.

[21] R. Huang, P.C.Y. Lee, W.-S. Lin, J.-D. Yu, Extensional, thickness-stretch and symmetric thickness-shear vibrations of piezoceramic disks, IEEE Transactions on Ultrasonics, Ferroelectrics and Frequency Control. 49 (2002) 1507–1515. https://doi.org/10.1109/tuffc.2002.1049732.

[22] P.C.Y. Lee, An accurate two-dimensional theory of vibrations of isotropic, elastic plates, Acta Mechanica Solida Sinica. 24 (2011) 125–134. https://doi.org/10.1016/s0894-9166(11)60014-1.

[23] N. Li, Z. Qian, J. Yang, Two-dimensional equations for piezoelectric thin-film acoustic wave resonators, International Journal of Solids and Structures. 110 (2017) 170–177. https://doi.org/10.1016/j.ijsolstr.2017.01.031.

[24] N. Li, Z. Qian, B. Wang, Forced coupling vibration analysis of FBAR based on two-dimensional equations associated with state-vector approach, AIP Advances. 8 (2018) 095306. https://doi.org/10.1063/1.5046533.

[25] N. Li, B. Wang, Z. Qian, I. Kuznetsova, T. Ma, Two-Dimensional Plate Theory for the Analysis of Coupling Vibrations in Shear Mode FBARs, IEEE Transactions on Ultrasonics, Ferroelectrics, and Frequency Control. 67 (2020) 1897–1908. https://doi.org/10.1109/tuffc.2020.2992287.

[26] D.J. Gorman, Free vibration analysis of the completely free rectangular plate by the method of superposition, Journal of Sound and Vibration. 57 (1978) 437–447. https://doi.org/10.1016/0022-460x(78)90322-x.

[27] D.J. Gorman, Free in-plane vibration analysis of rectangular plates by the method of superposition, Journal of Sound and Vibration. 272 (2004) 831–851. https://doi.org/10.1016/S0022-460X(03)00421-8.

[28] D.J. Gorman, Accurate in-plane free vibration analysis of rectangular orthotropic plates, Journal of Sound and Vibration. 323 (2009) 426–443. https://doi.org/10.1016/j.jsv.2008.12.021.

[29] D. Royer, E. Dieulesaint, Elastic waves in solids I: Free and guided propagation, Springer Science & Business Media, 1999.

[30] T. Senjuntichai, W. Kaewjuea, R.K.N.D. Rajapakse, Piezoelectric cylinder under voltage and axial loading, International Journal of Applied Electromagnetics and Mechanics. 27 (2008) 93–116. https://doi.org/10.3233/JAE-2008-923.

[31] M. Abramowitz, I.A. Stegun, Handbook of mathematical functions with formulas, graphs, and mathematical tables, US Government printing office, 1948.

[32] E.W. Weisstein, Cubic formula, Https://Mathworld. Wolfram. Com/. (2002).

[33] H.F. Tiersten, Linear Piezoelectric Plate Vibrations, Springer, 1969. https://doi.org/10.1007/978-1-4899-6453-3.

[34] D. Kim, M. Kim, K. Kang, K. Son, S. Lee, Coupled vibration analysis for a piezoelectric array element using superposition method, in: 2013 IEEE International Ultrasonics Symposium (IUS), IEEE, 2013: pp. 2179–2182. https://doi.org/10.1109/ultsym.2013.0557.

[35] S. Kevorkian, M. Pascal, An accurate method for free vibration analysis of structures with application to plates, Journal of Sound and Vibration. 246 (2001) 795–814. https://doi.org/10.1006/jsvi.2001.3709.

[36] Ferroperm piezoceramic material data for modelling. https://www.meggittferroperm.com/resources/data-for-modelling/.

[37] D. Wang, H. Zhu, Monitoring of the strength gain of concrete using embedded PZT impedance transducer, Construction and Building Materials. 25 (2011) 3703–

3708. https://doi.org/10.1016/j.conbuildmat.2011.04.020.

[38] J. Kocbach, Finite element modeling of ultrasonic piezoelectric transducers, PhD Thesis, University of Bergen, 2000.

[39] S. Ikegami, I. Ueda, S. Kobayashi, Frequency spectra of resonant vibration in disk plates of PbTiO3 piezoelectric ceramics, The Journal of the Acoustical Society of America. 55 (1974) 339–344. https://doi.org/10.1121/1.1914508.

[40] N. Guo, P. Cawley, Measurement and prediction of the frequency spectrum of piezoelectric disks by modal analysis, The Journal of the Acoustical Society of America. 92 (1992) 3379–3388. https://doi.org/10.1121/1.404188.

[41] V. Dimi, M. Radmanovi, Resonance frequencies of PZT piezoceramic disks: a numerical approach, Facta Universitatis-Series: Mechanics, Automatic Control and Robotics. 3 (2002) 431–442.